



Preparation of lanthanide-doped polystyrene/CeO₂ abrasives and investigation of slurry stability and photochemical mechanical polishing performance

Yongyu Fan ^{a,b}, Jie Jiao ^{a,b}, Lang Zhao ^{a,*}, Jinkui Tang ^{a,b,**}

^a State Key Laboratory of Rare Earth Resource Utilization, Changchun Institute of Applied Chemistry, Chinese Academy of Sciences, Changchun, Jilin 130022, PR China

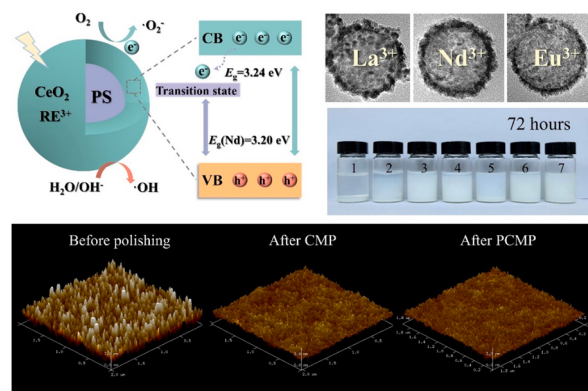
^b School of Applied Chemistry and Engineering, University of Science and Technology of China, Hefei, Anhui 230026, PR China



HIGHLIGHTS

- Synthesized RE³⁺ doped PS-CeO₂ core-shell abrasives for polishing of silicon wafer.
- Addressed the issue of abrasive agglomeration by adding dispersants.
- The polishing rate of Nd-doped abrasives is increased by 163 % under UV, and the roughness can be reduced from 0.82 nm to 0.36 nm.

GRAPHICAL ABSTRACT



ARTICLE INFO

Keywords:
Cerium oxide (CeO₂)
Polystyrene (PS)
Lanthanide doping
Chemical mechanical polishing (CMP)

ABSTRACT

With the pursuit of high efficiency and quality chemical mechanical polishing (CMP), exploring additional efficiency enhancement means based on the CMP has become a trend. Polystyrene/CeO₂ core-shell abrasives (core: 85 nm, shell: 10 nm) doped with Lanthanide (La, Nd, and Eu) were synthesized by a modified in situ chemical precipitation method, promising application for photocatalytic-assisted CMP of silica wafer. The doping of La, Nd, and Eu can reduce the band gap of CeO₂ from 3.24 eV to 3.23 eV, 3.20 eV, and 3.22 eV, respectively, indicating enhanced photocatalytic activity. Especially for Nd-doped abrasives, the content of Ce³⁺ increases from 0.49 to 0.56, accompanied by the generation of oxygen vacancies, as proved by X-ray photoelectron spectroscopy (XPS) and Raman spectra. In addition, the prepared polishing slurry could remain stable for up to 7 days by the steric hindrance effect and electrostatic repulsion of the dispersants. The materials removal rate of Nd-doped abrasive in photocatalytic-assisted CMP of SiO₂ films reaches 174.3 ± 7.6 nm/min, which is 163% higher than those in CMP, while the surface roughness (Ra) in localized areas ($2 \times 2 \mu\text{m}^2$) can be reduced from the

* Corresponding author.

** Corresponding author at: State Key Laboratory of Rare Earth Resource Utilization, Changchun Institute of Applied Chemistry, Chinese Academy of Sciences, Changchun, Jilin 130022, PR China.

E-mail addresses: fystc@ciac.ac.cn (Y. Fan), zhaolang@ciac.ac.cn (L. Zhao), tang@ciac.ac.cn (J. Tang).

initial 0.82 ± 0.01 nm to 0.36 ± 0.05 nm. Detailed reaction and removal mechanism involved in photocatalytic-assisted CMP processes is discussed.

1. Introduction

Chemical mechanical polishing (CMP) is a nanoscale material removal technique by the dual action of chemical etching and mechanical grinding to obtain smooth surfaces. It is an effective tool for global planarization at the nanoscale and atomic scale [1]. However, toxic and polluted ingredients are usually employed in traditional CMP, resulting in pollution to the environment [2]. To overcome this challenge, novel green CMP is developed for copper [3], diamond [4], alloys [5], and sapphire [6], which is for use in high-performance devices of semiconductor, optoelectronics, and microelectronics industries. The most important is that these studies are a great contribution to the environment, dramatically reducing pollution to the environment [7]. Cerium oxide, as one of the mainstream polishing materials, the Ce-OH group on the surface can react with the Si-O⁻ site on the SiO₂ to form Ce-O-Si, which is stronger than the Si-O-Si, so that the SiO₂ can be easily removed under mechanical force, and this is "Chemical tooth" model proposed by Cook [8]. In addition, the electronic structure of cerium is [Xe]4f¹5d¹6s², determining the unique reversible Ce³⁺/Ce⁴⁺ redox pair and adjustable oxygen vacancies, facilitating high-performance redox processes and catalytic reactions. Given the above, CeO₂ has become a key research target for novel abrasives [9].

With cross-disciplinary applications in different fields, the synthesis of polishing materials is no longer limited to single species, and the use of coatings and doping to prepare composite abrasives has been a critical trend in the CMP field [10]. Since the growth of CeO₂ nanoparticles is almost uncontrolled, Chen Yang et al. [11–15] coated CeO₂ on the surface of PS and polymethyl methacrylate (PMMA) polymers and significantly reduced the surface roughness by utilizing these low elastic modulus organic cores. Cheng et al. [16,17] performed (La, Nd, and Yb) ion doping in commercial CeO₂ by an initial impregnation method to promote the formation of oxygen vacancies and the conversion of Ce⁴⁺ to Ce³⁺. As for Nd/CeO₂, the polishing rate of silica was accelerated by 29.6%, and a better surface quality (Sa = 9.6 Å) was obtained. Gao Bo et al. [18] inserted TiO₂ into the PS-CeO₂ system to realize the spatial separation of redox species with the help of heterojunction structure for enhancing the photocatalytic activity, yielding the material removal rate (MRR) of 1.223 μm/h and Ra of 0.497 nm. Chen Ailian et al. [14,19] designed mesoporous SiO₂-CeO₂ core-shell particles doped with Sm³⁺ or Er³⁺ [20,21], raising the polishing rate by 36% and 160%, respectively. Nevertheless, the SiO₂ was prepared in extremely unproductive yield, and the treatment was complicated. In summary, the design of the shell-core structure may reduce the Ra; doping and compounding can promote the MRR [22–25].

In addition, the agglomeration of slurry is one of the burning questions to be addressed in CMP. However, the existing reports on CeO₂ composite abrasives seldom mention the slurry formulations and actual stabilization effects. In this work, CeO₂ was coated on the PS surface to synthesize PS/CeO₂, which is noted as PS-Ce; lanthanide RE (RE = La, Nd, Eu) were selected as the dopants, and the synthesized PS/CeO₂/RE particles are named as PS-Ce-La, PS-Ce-Nd, and PS-Ce-Eu, respectively. The organic PS as the core could lessen the abrasive hardness to minimize the scratch. Simultaneously, ion doping in the shell layer aims to reinforce the CeO₂ photocatalytic reaction activity for an enhanced polishing rate. Subsequently, the selection of slurry components is managed, metal ions are eliminated, and the organic alkali, a nontoxic and harmless, is used as a pH regulator. Aiming to design innovative composite abrasives, develop environmentally friendly, metal ion-free, and highly dispersed CMP slurry, and establish a systematic and complete formula development program for PCMP.

2. Materials and methods

2.1. Materials

Monomer styrene (St) was supplied by Aladdin Reagent Co., potassium persulfate (KPS), cerium nitrate hexahydrate (Ce(NO₃)₃·6H₂O), lanthanum nitrate hexahydrate (La(NO₃)₃·6H₂O), neodymium nitrate hexahydrate (Nd(NO₃)₃·6H₂O), europium nitrate hexahydrate (Eu(NO₃)₃·6H₂O), sodium dodecyl sulfate (SDS), ammonium dodecyl sulfate (ALS), polyvinylpyrrolidone (PVP) and polyethylene glycol (PEG 20000) were all obtained from Shanghai Maclean Biochemical Technology Co., Primary Alcohol Ethoxylate (AEO-7) was acquired from Shanghai Dingfen Chemical Technology Co., hexamethylenetetramine (HMT) was purchased from Sinopharm Group Chemical Reagent Co., all chemicals were of analytical grade.

2.2. Synthesis of composite particles

Monodisperse PS was prepared by soap-free emulsion polymerization [26,27]: in a double-necked round-bottom flask, 200 ml of deionized (DI) water was added and bubbled with nitrogen for 30 min. Subsequently, 6 ml of St and 0.28 g of SDS were added under magnetic stirring. The mixture was heated to 70 °C, and 40 ml of KPS solution (0.15 wt%) was slowly added to initiate polymerization. The reaction was carried out for 8 h.

The preparation of core-shell abrasives: 8 g of PS was dissolved in 200 ml of DI, sonicated for 20 min, and then heated to 75 °C. After that, 2 g of HMT, 0.8 g of Ce(NO₃)₃·6H₂O, and 0.2 g of Nd(NO₃)₃·6H₂O were added, and the reaction was carried out for 3 h. The precipitate was filtered and washed several times with deionized and ethanol and dried at 80 °C for 4 h to obtain doped modified PS-Ce-Nd composites. The undoped and remaining doped core-shell materials were synthesized via a similar procedure.

2.3. hydroxyl radical trapping test

The activity of the photocatalytic reaction can be evaluated by the amount of hydroxyl radicals (·OH) produced during the process, however, it cannot be directly detected. Some researchers [28–30] demonstrated that Congo red (CR) can be degraded by ·OH (·OH can be trapped by CR), leading to a lower absorbance of CR (measured by the UV-vis spectrophotometer), which indirectly reflected the production of ·OH [18]. In this work, 0.012 g of sample was mixed with 12 ml of CR solution (210 mg·L⁻¹) and sonicated for 15 min under dark conditions to exclude the decrease in CR absorbance caused by adsorption. Subsequently, the mixture was illuminated under a Xenon lamp (365 nm) for 1 h trapping test.

2.4. Stability experiment

Preparation of polishing slurry: 1 g of PS-Ce-Nd was dispersed in 100 g of DI, then 1 g of the surface active agent (SAA) was added, which include PEG, EG, AEO-7, ALS, and PVP, and details are given in Table 3. Subsequently, aminomethyl propanol (AMP) was used to adjust pH to 10, and the solution was distributed by ultrasonication for 4 h and left to settle. The photograph of different periods recorded the settling. Before measuring Zeta and particle size distribution, the polishing liquids must be diluted 5 times with the same solvent to ensure the surfactant concentration and pH remain fixed.

2.5. Polishing tests

Add 1 g of PS-Ce-Nd and 1 g of PVP to 100 ml of DI and adjust the pH to 10 with AMP. The polishing experiments were carried out by Bruker Universal Mechanical Tester (UMT Tribolab). The pad and wafer were rotated at 90 and 120 r/min, the slurry injection rate was 100 ml/min, the polishing pressure was 6 N, and the time was 1 min. The UV-assisted polishing experiments were performed with an OLED lamp (20 W) as the light source ($\lambda = 365$ nm), and the slurry was light-treated for 1 h before polishing. The silicon wafers to be polished were thermally oxidized with an oxide layer thickness of 1000 nm, which were processed into small rectangular pieces of 1.5 cm \times 2.0 cm. After polishing, the silica wafers were sonicated with SC1 ($\text{NH}_3\cdot\text{H}_2\text{O}/\text{H}_2\text{O}_2/\text{H}_2\text{O} = 1:1:5$) cleaning solution, deionized water, and ethanol, then dried with pure N_2 . The workpiece mass was weighed by ultra-precision electronic balance (XS105, Mettler Toledo, exact to 0.01 mg), and the MRR (nm/min) was calculated as follows [12].

$$\text{MRR} = \frac{m_0 - m}{\rho \cdot S \cdot t} \quad (1)$$

where m_0 and m are the masses before and after polishing, ρ is the oxide layer density (2.2 g/cm³), S is the surface area of the polished wafer, and t is the polishing time. The surface morphology of the wafers was analyzed by atomic force microscopy (AFM, Nanoman VS) with a scanning range of $2 \times 2 \mu\text{m}^2$ in tap mode. The AFM probe (OLTESPA-R3) has a cantilever resonance frequency of 70 kHz (in the air), an elasticity factor of 2 N/m, and a tip radius of curvature of 7 nm.

2.6. Characterization

The crystal structures were recorded on a powder X-ray diffractometer with Cu K α radiation ($\lambda = 1.4518 \text{ \AA}$) at a scanning rate of $0.15^\circ/\text{s}$ over the 2θ ranging from 10° to 90° . The surface morphology of synthesized products was analyzed by a field emission scanning electron microscopy (SEM, Hitachi S4800). The internal structure and elemental distribution were observed by transmission electron microscopy (TEM, JEOL JEM-2010 EX). For SEM and TEM observations, the sample was dispersed in ethanol by ultrasonic treatment and then dropped onto silica wafer and Cu grids, respectively. Ultraviolet-visible diffuse reflectance spectra (UV-vis DRS) was conducted using Shimadzu UV-3600. Photoluminescence spectra (PL) were acquired by a Modular Spectrofluorometer Fluorolog 3 (excitation at 404 nm, Split width: 5 nm). X-ray photoelectron spectroscopy (XPS) was obtained by PHI-5000 Versaprobe III spectrometer with Al K α radiation ($h\nu = 1486.6$ eV). The formation of oxygen vacancies was characterized using

Raman spectroscopy (HORIBA T64000) with tests ranging from 400 to 700 nm. Particle size distribution based on the dynamic light scattering (DLS) method and Zeta potential of slurry were examined by a Zetasizer Nano ZS (Malvern Instruments, UK).

3. Results and discussion

3.1. Structural characteristics

Wide-angle XRD patterns of the as-prepared materials are depicted in Fig. 1(a). The characteristic diffraction peaks located at $2\theta = 28.6^\circ, 33.1^\circ, 47.5^\circ, 56.9^\circ, 59.4^\circ, 69.7^\circ, 77.0^\circ$, and 79.5° can be indexed to the lattice planes of (111), (200), (220), (311), (222), (400), (331) and (420) reflections of cubic fluorite-type phase CeO₂ (JCPDS No. 34-0394). Furthermore, a broad peak of amorphous PS is observed around $2\theta = 15\text{--}25^\circ$, while the typical peaks of La₂O₃, Nd₂O₃, and Eu₂O₃ cannot be detected, suggesting no secondary phase formed. Yet all peaks are shifted obviously to a lower 2θ angle after doping, as clearly shown in Fig. 1(b), confirming successful RE³⁺-doping in CeO₂ lattices. Likewise, the ionic radius of La³⁺ (106 pm), Nd³⁺ (99.5 pm), and Eu³⁺ (95.0 pm) are slightly larger than that of Ce⁴⁺ (92.0 pm), so lattice expansion is expected, and peak shift is exhibited after the replacement of Ce⁴⁺ with larger RE³⁺. According to the Bragg equation (Eq. 2) [31], unit cell lattice parameters (a, b, c) values and crystal spacing can be calculated from (111) XRD data. The results (Table 1) show that full width at half maximum (FWHM) of diffraction peak increases, and the interplanar spacing more or less reduces after doping. Moreover, the average grain size for PS-Ce-La, PS-Ce-Nd, and PS-Ce-Eu is 5.963 nm, 6.901 nm, and 6.132 nm, respectively, which are smaller than PS-Ce (8.304 nm) based on the calculation of the Debye-Scherrer formula (Eq. 3) [31].

$$2d \sin \theta = n\lambda \quad (2)$$

$$D = K\lambda / (\beta \cos \theta) \quad (3)$$

Here, d is interplanar spacing, θ is the angle between the incident X-

Table 1
Properties of the Ceria-based composite particles by XRD.

Lattice	PS-Ce	PS-Ce-La	PS-Ce-Nd	PS-Ce-Eu
2 Theta	28.67	28.59	28.44	28.52
FWHM	0.976	1.359	1.174	1.321
Crystal spacing (Å)	3.110	3.119	3.134	3.126
Lattice constant (Å)	5.387	5.402	5.429	5.414
Average grain size (nm)	8.304	5.963	6.901	6.132

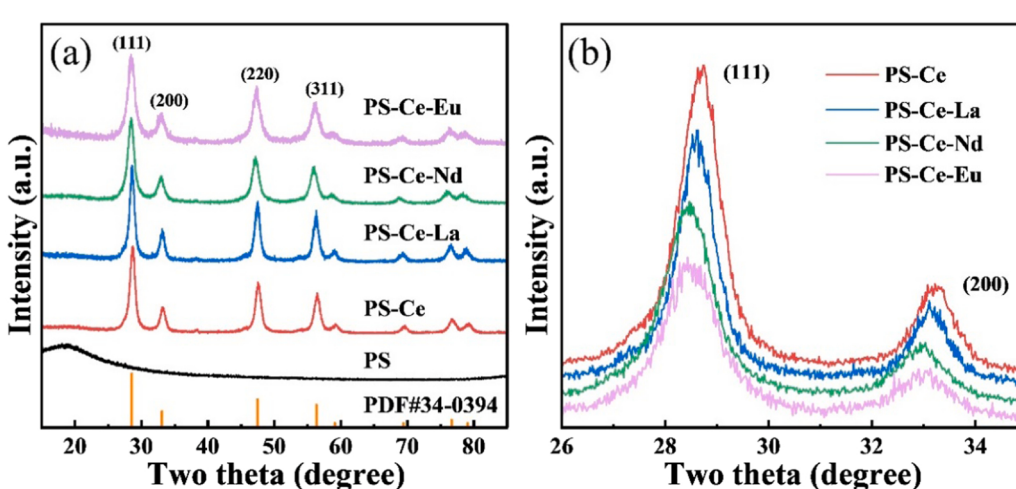


Fig. 1. XRD patterns of (a) PS and core-shell nanocomposites; (b) enlarged drawing of (111) and (200) lattice plane.

rays and the corresponding crystal plane, λ is the wavelength of X-rays ($\lambda = 0.15406$ nm), n is the number of diffraction levels, D is average grain size, β is FWHM, and K is 0.89.

Fig. 2(a) demonstrates that PS nanoparticles are spherical with an average size of about 85 nm and have a smooth surface with a high degree of monodispersity, which is conducive to the subsequent preparation of high-quality composite material. In contrast, the surfaces of four abrasives, PS-Ce (**Fig. 2b**), PS-Ce-La (**Fig. 2c**), PS-Ce-Nd (**Fig. 2d**), and PS-Ce-Eu (**Fig. 2e**), become relatively rough, yet the initial spherical morphology can still be well maintained.

The internal structure of the composites can be viewed from the TEM results in **Fig. 3**. In the case of PS-Ce, the core particle size is about 85 nm, and the shell thickness is 10 nm. As seen in **Fig. 3(b)**, the shell layer of PS-Ce-La particles is mainly attached to the PS surface as a block material with a strawberry-like surface. The remaining two doped particles (**Fig. 3c-d**) have a complete coating; the only difference is the thickness of the outer shell. Combined with the high-resolution TEM, the crystalline spacing of CeO₂ has increased to varying degrees after doping, which is in harmony with the XRD analysis.

A TEM energy spectrum analysis is performed to illustrate better ion doping and the distribution of various elements on individual particles (**Fig. 4**). The findings suggest a significant uplift in the curves of La, Nd, and Eu at the boundaries of the particles. In contrast, the distributions of Ce and O display a similar groove-like pattern. However, the C is located in the internal area. The above outcomes prove the successful formation of the shell-core composites and the efficient doping of rare earth ions.

The photoluminescence spectra of PS-Ce and doped nanoparticles measured using the excitation wavelength of 404 nm are shown in **Fig. 5**. A broad emission band is observed from 400 to 500 nm with different peak positions, which may be attributed to the jump in defect levels in the Ce 4 f to O 2p band range [32]. It is universally accepted that the intensity of PL is positively associated with the chance of recombination of excited electrons and holes, and a decrease in luminescence intensity implies a reduction in the rate of combination of electron-hole pairs [33]. Compared with PS-Ce, the decorated particles exhibit a relatively low luminescence intensity at room temperature, substantiating the resultful separation of electron-hole pairs and the enhanced photocatalytic activity.

For the synthesized abrasives, the optical properties can also be

evaluated by UV-vis diffusion absorption spectroscopy. As displayed in **Fig. 6(a)**, the strong absorption properties exhibited at 340 nm may be due to the electronic transition from O 2p to Ce 4f levels. The wavelength thresholds (λ_g) of PS-Ce-La (407 nm), PS-Ce-Nd (419 nm), and PS-Ce-Eu (412 nm) are shifted to a higher wavelength compared to the undoped ones (405 nm), indicating the enhanced light absorption ability. In addition, the band gap (E_g) of abrasives is calculated in terms of the Schuster-Kubelka-Munk function (**Eq. 4**) [34].

$$(\alpha h\nu)^n = A(h\nu - E_g) \quad (4)$$

Here, α is the absorption coefficient, $h\nu$ is the discrete photon energy, and n is taken as 2 (CeO₂ is a direct gap semiconductor). The plots of $(\alpha h\nu)^2$ versus $h\nu$ are shown in **Fig. 6(b)**, which reveals that the E_g values of PS-Ce-La, PS-Ce-Nd, and PS-Ce-Eu are 3.23, 3.20, and 3.22 eV, respectively, indicating that RE-doping can induce the narrowed E_g of PS-Ce (3.24 eV). The narrowing of the E_g may be attributed to surface defects in the CeO₂ lattice caused by doping (details in **Section 3.4**). Above all, PS-Ce-Nd exhibits the lowest E_g and the highest λ_g , implying the most excellent photocatalytic activity. Therefore, PS-Ce-Nd is finally chosen to prepare the polishing slurry and further investigate its stability and polishing performance.

The results of hydroxyl radical trapping test are shown in **Fig. 7(a)**, CR exhibits an absorbance peak at ca. 496 nm and the absorbance at 0 min is varied, which is caused by the different physical adsorption capacities of the abrasives. After 60 min trapping, the absorbance of CR is decreased, and the degradation of CR by PS-Ce-Nd is significantly superior to that by PS-Ce. According to **Section 2.3**, it is known that PS-Ce-Nd possesses enhanced photocatalytic activity which is consistent with the results of DRS. In short, the hydroxyl radical trapping test proved that both abrasives can produce ·OH during the photocatalytic reaction, which is also an essential basis for uncovering the mechanism of PCMP in later sections.

Raman spectra (**Fig. 7b**) display a distinct peak at 460 cm⁻¹, corresponding to the typical Raman vibration mode (F_{2g}) of the cubic fluorite-type CeO₂ [24]. The peak shifts to lower wave numbers after Nd doping, possibly due to the increase of Ce³⁺ [35]. Moreover, the peaks at ca. 560 cm⁻¹ can be ascribed to extrinsic defects caused by Nd doping. It is generally accepted that the ratio of the peak intensity at 560 cm⁻¹ and 460 cm⁻¹ (I_{560}/I_{460}) reflects the concentration of oxygen vacancies (V_O)

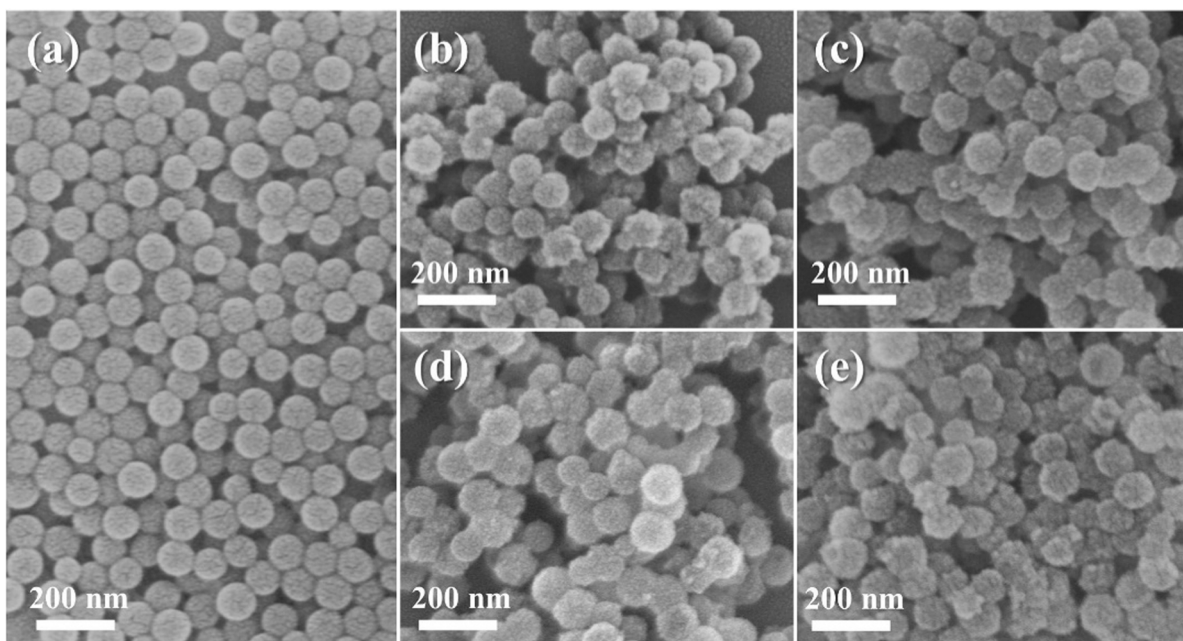


Fig. 2. FESEM images of (a) PS, (b) PS-Ce, (c) PS-Ce-La, (d) PS-Ce-Nd, and (e) PS-Ce-Eu.

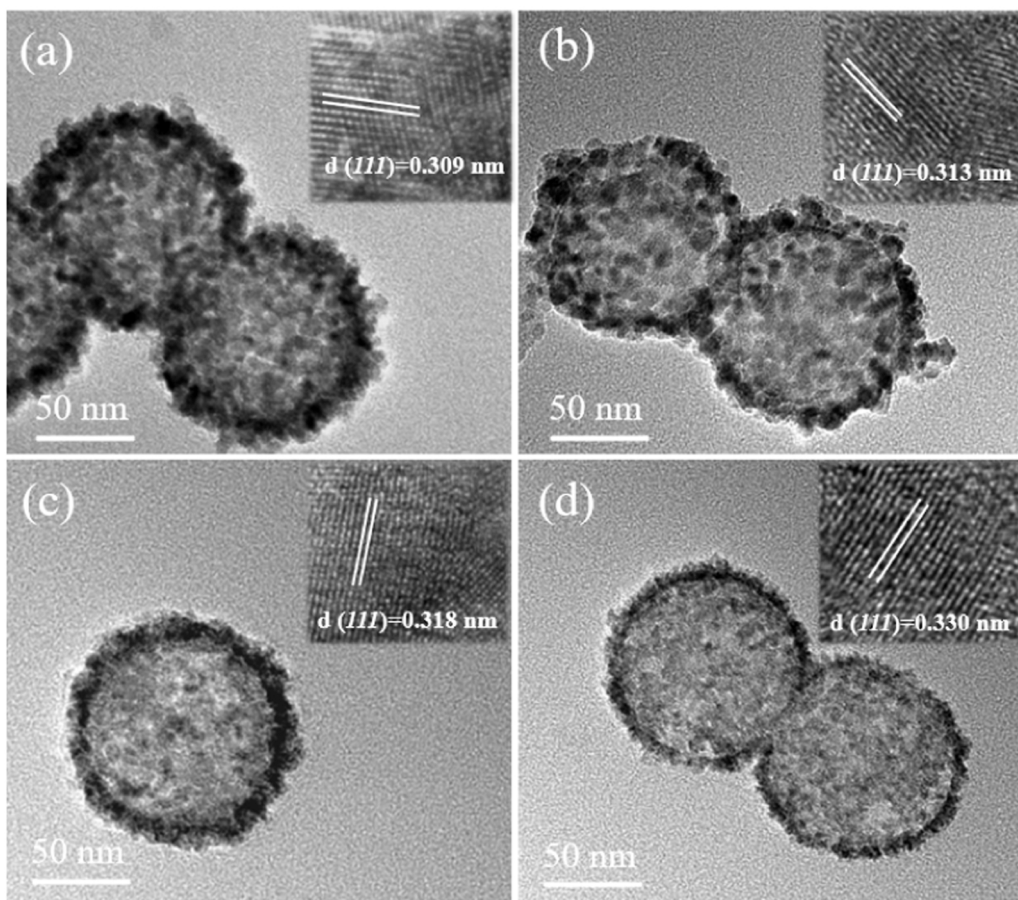


Fig. 3. Low- and high-resolution TEM images of (a) PS-Ce, (b) PS-Ce-La, (c) PS-Ce-Nd, and (d) PS-Ce-Eu.

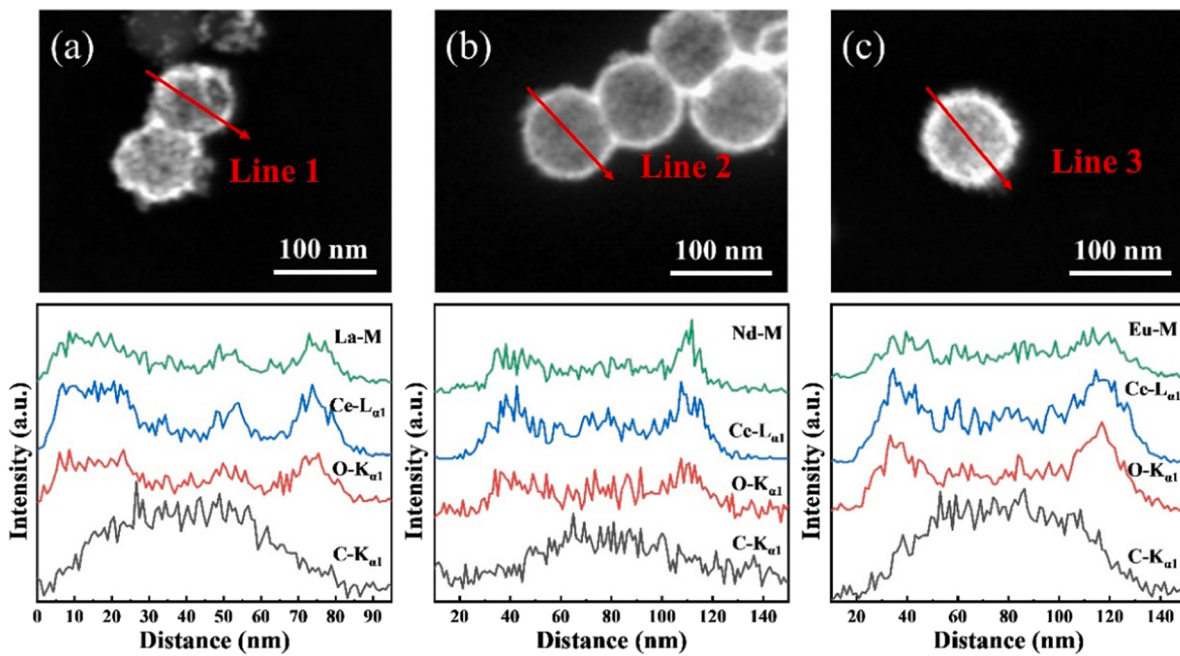


Fig. 4. The element distribution profile of the red line indicated in the TEM image: (a) PS-Ce-La, (b) PS-Ce-Nd, and (c) PS-Ce-Eu.

in CeO_2 [36]. The calculated value for PS-Ce-Nd (ca. 0.22) is higher than that of PS-Ce (ca. 0.11), implying increased V_O after doping.

The surface elemental composition and valance states of PS-Ce-Nd

and PS-Ce are analyzed by XPS spectroscopy. The full survey spectrum (Fig. 8a) confirms the presence of Ce, O, and C elements. As seen from the high-resolution Nd 3d core level spectra (Fig. 8c), the peaks at ca.

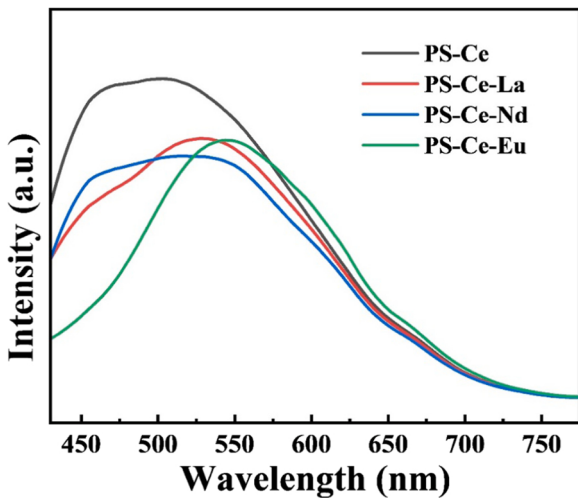


Fig. 5. Photoluminescence spectra of the synthesized abrasive grains. Excitation at 404 nm. Split width: 5 nm.

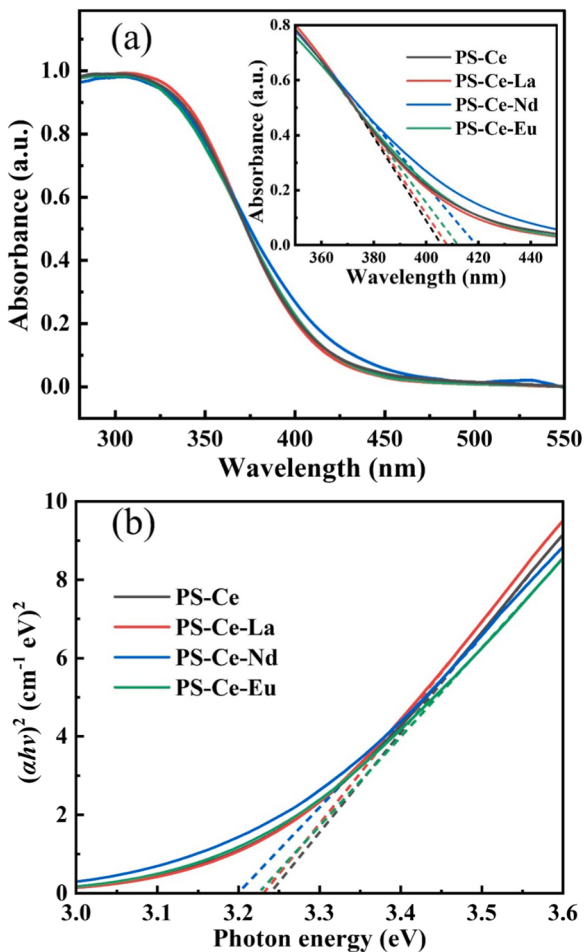


Fig. 6. (a) UV-vis absorption spectra and (b) plots of $(\alpha h\nu)^2$ versus $h\nu$ of Ceria-based composites.

1004.9 eV and 982.6 eV can be assigned to the Nd 3d_{3/2} and 3d_{5/2} contributions, revealing the successful doping of Nd³⁺. Moreover, the Ce³⁺ content in CeO₂ could be calculated by peak deconvolution of the XPS spectrum, and Fig. 8(b, d) exhibit ten deconvoluted peaks (labeled as v and u group) obtained after the treatment. The valence states,

binding energy (BE), and peak area corresponding to the deconvoluted peaks are provided in Table 2. The concentration of Ce³⁺ can be calculated according to the equations (Eqs. 5–7) [16,21,24], here C and A represent concentration and area.

$$C(Ce^{3+}) = \frac{A(Ce^{3+})}{A(Ce^{3+}) + A(Ce^{4+})} \quad (5)$$

$$A(Ce^{3+}) = A(v_0) + A(v') + A(u_0) + A(u') \quad (6)$$

$$A(Ce^{4+}) = A(v) + A(v') + A(v'') + A(u) + A(u') + A(u'') \quad (7)$$

The Ce³⁺ ratios of PS-Ce and PS-Ce-Nd are calculated to be 49% and 56%, respectively, confirming that increased Ce³⁺ content in CeO₂ lattice after the doping of Nd³⁺. The results of Raman and XPS spectroscopy more directly demonstrate the formation of V_O and the conversion of Ce⁴⁺ to Ce³⁺ due to doping, which also provide convincing grounds for constructing an obvious connection between the structural characterization of the material synthesis (Ce³⁺, V_O, etc.) with CMP/PCMP performance.

3.2. Polishing slurry stability

The dispersion stability of the abrasives can be improved by adding surfactants, which lessens the adverse effects of abrasive agglomeration on polishing. Fig. 9 shows the variation of different polishing slurries over 14 days. No. 1 is left untreated with a pH of about 5. The additives of the remaining solutions are detailed in Table 3, where the content of PS-Ce-Nd and surfactants are 1 wt%, and pH is adjusted with AMP.

DLS particle-size distribution plays a vital role in slurry stability evaluations. It is usually believed that the smaller the average size and span ($(D_{90}-D_{10})/D_{50}$), the better the dispersibility. Here, D_i represents the particle size corresponding to a sample with a cumulative percent size distribution of i %. As shown in Table 2, the average size of abrasives in DI is as high as 1328 nm (NO.1), indicating severe agglomeration. AEO-7 (NO.5) exhibits slight improvement, but still reaches 836 nm and settles in a very short time, which coincides with the phenomenon in Fig. 9. Adjustment of pH (NO.2) reduces the average size to 534 nm, but the span is up to 1.71, suggesting a wide range of size distribution and retention of extremely agglomerated particles. It is also observed in PEG (NO.3) and EG (NO.4), indicating that PEG and EG contribute nothing to the dispersion of the slurry. Fortunately, ALS (NO.6) and PVP (NO.7) presents excellent results. The reason for the above phenomenon may be related to another evaluation indicator, Zeta potential.

The Zeta potential of the particle surface can be regulated by the pH and surfactants. The larger the absolute value of potential, the more charge on the surface of the particles, thus enabling the particles to achieve outstanding dispersion stability via electrostatic repulsion. With only pH adjustment (Table 3), the Zeta potential of NO. 2 shifts from 13.2 mV to -31.8 mV, and the stability is visually enhanced. Comparing the effect of different dispersants, No. 6 (ALS) and No. 7 (PVP) achieve excellent dispersion performance and remain remarkably stable for 7 days. The reasons may be that ALS, an anionic surfactant, can alter the charge distribution in solution and reinforce the Zeta potential of the particle surface (-33.6 mV) to promote the stability of polishing slurry by electrostatic repulsion mechanism. Furthermore, PVP is a non-ionic surfactant whose hydrophilic group can be adsorbed by the high surface energy PS-Ce-Nd to form a polymer adsorption layer on the particle surface that utilizes the steric hindrance effect. Hence, it dramatically boosts the stability of the polishing slurry even though the Zeta potential is reduced to -12.3 mV.

In summary, the ionic dispersant mainly achieves the dispersion stabilization of polishing slurry via electrostatic stabilization, while the non-ionic dispersant works by steric hindrance. According to the results of stability experiments, PVP is selected to prepare the slurry for investigating the polishing performance of PS-Ce-Nd abrasive.

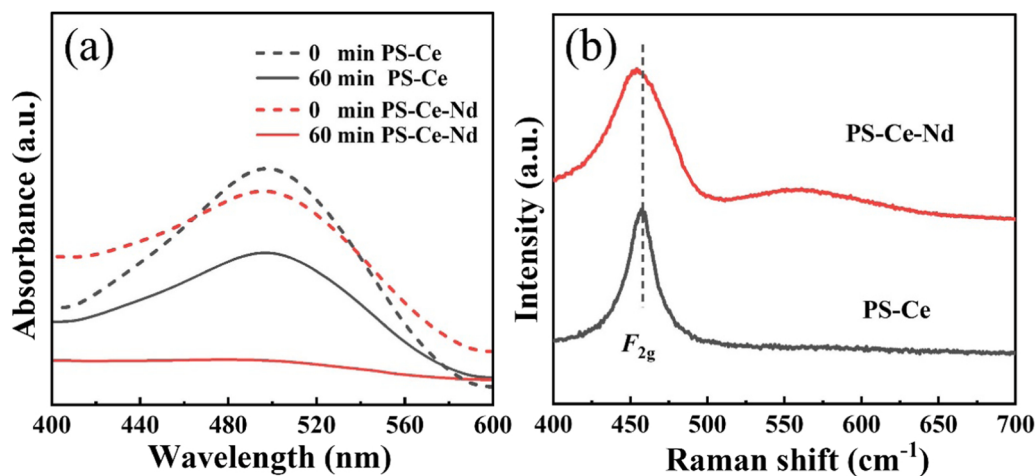


Fig. 7. (a) Absorbance of CR after photocatalytic reaction by PS-Ce and PS-Ce-Nd. (b) Raman spectra of PS-Ce and PS-Ce-Nd.

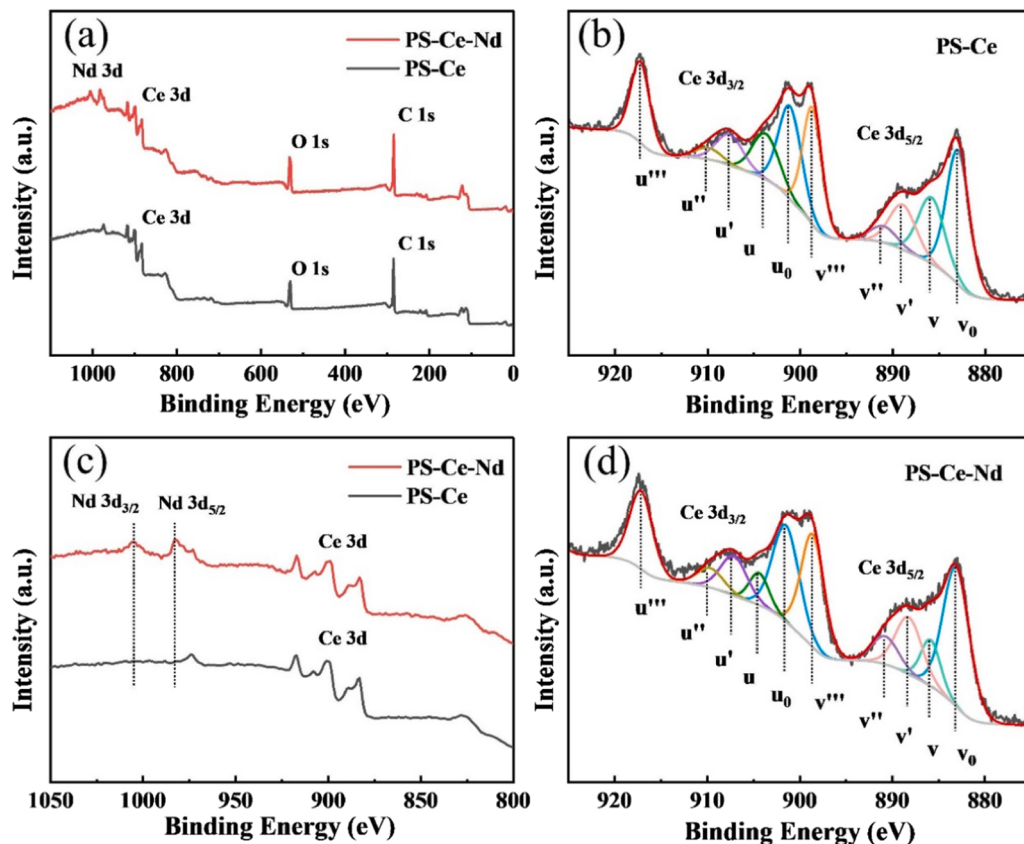


Fig. 8. XPS spectra results of PS-Ce and PS-Ce-Nd: (a) full survey spectrum, (c) Nd 3d, and (b, d) Ce 3d core level spectra.

Table 2
the oxidation states, the binding energies, and the peak areas of Ce species for PS-Ce and PS-Ce-Nd.

	Ce ³⁺				Ce ⁴⁺						Ce ³⁺ content
	v ₀	v'	u ₀	u'	v	v''	v'''	u	u''	u'''	
PS-Ce											
BE (eV)	883.0	888.9	901.1	907.6	885.8	891.0	898.7	903.7	909.9	917.3	
Area	39399	15200	27282	10526	22390	5598	28360	15504	3876	19638	0.49
PS-Ce-Nd											
BE (eV)	883.1	888.2	901.5	907.1	885.9	890.8	898.7	904.4	909.7	917.2	
Area	47075	19359	32598	13405	11585	9503	30716	8022	6580	21269	0.56

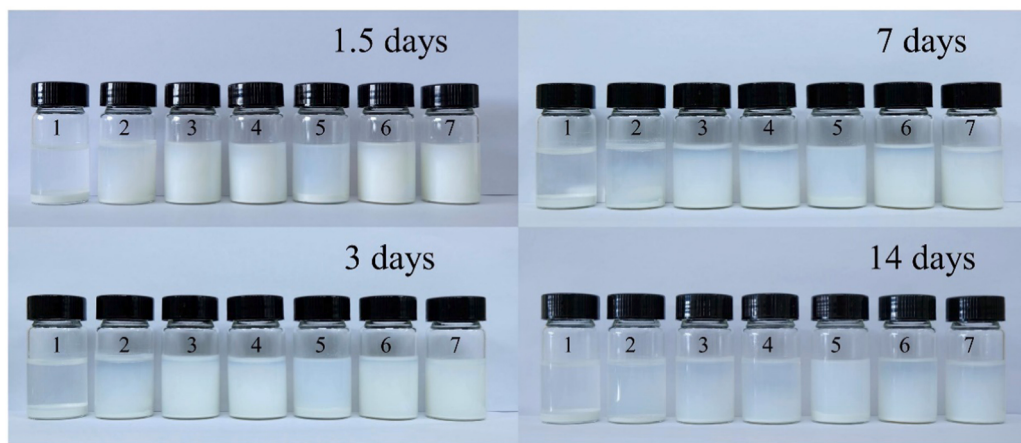


Fig. 9. Stability of PS-Ce-Nd slurry at different times.

Table 3
Zeta potential of La-Ce-Nd slurry with different dispersants.

	1	2	3	4	5	6	7
SAA			PEG	EG	AEO-7	ALS	PVP
pH	5	10	10	10	10	10	10
Zeta potential (mV)	13.2	-31.8	-24.7	-39.2	-21.7	-33.6	-12.3
Average size (nm)	1328	534	335	691	836	381	330
span	0.41	1.71	1.78	1.67	0.62	0.45	0.64

3.3. Polishing tests

AFM can monitor the silica wafer surface topography, and subsequent data processing using the software can yield the corresponding surface roughness and cross-sectional profile, which will serve as powerful indicators for evaluating the polishing performance of CMP and PCMP.

Fig. 10 (a) depicts the original surface of the silica wafer where a large number of rough peaks at the nanoscale exist. Fig. 10 (b) and (c) respond to the CMP and PCMP results of PS-Ce-Nd abrasives, respectively, in which most rough peaks have been removed and highly flat surfaces are obtained. These three-dimensional (3D)-AFM images provide direct evidence of the surface morphology variations caused by CMP and PCMP, initially justifying the polishing effect of the abrasives.

Fig. 11 shows typical 2D-AFM images of the substrate surface before and after polishing. Compared to pre-polishing, the AFM height images of the polished wafer surface are more uniform in color, which generally suggests better surface quality and flatness. The obtained roughness is summarized in Table 4, revealing that the original surface roughness is up to 0.82 nm, and it is reduced to 0.46 and 0.36 nm after CMP and PCMP of PS-Ce-Nd abrasives, respectively. In addition, cross-sectional traces along arbitrary delineations in the 2D AFM images are further

explored for topographic variation. For the initial surface, the line traces (Fig. 11 a) indicate a maximum peak height close to 6 nm, a maximum valley depth up to 3 nm, and a corresponding roughness of about 1.5 nm, with a highly uneven surface. In CMP applications (Fig. 11 b), the maximum peak height and valley depth can be effectively reduced to less than 1 nm, and for PCMP (Fig. 11 c), to less than 0.5 nm. In summary, no matter the surface morphology comparison or roughness and cross-sectional analysis confirm that the introduction of UV-assisted helps to reduce the topographic variation and optimize the polishing quality compared to CMP, even though further optimization of the polishing process is still needed to reduce the scratches in some areas.

On the other hand, the material removal rates of CMP and PCMP achieved by the composite PS-Ce-Nd are shown in Table 4. It indicates that UV photocatalysis effectively increased the polishing rate of Nd-doped abrasives from 65.8 to 174.3 nm/min, which increased by 163%. The possible reasons and polishing mechanisms will be described in detail in the next section.

The proposed PS-Ce-Nd abrasive is compared with pure CeO₂ and previously reported abrasives on silica wafer, and the corresponding results of MRR and surface roughness (RMS: root mean square) are summarized in Table 5. Higher MRR and lower surface roughness in CMP are desired, yet they often existed as a pair of oxymorons. It can be clearly seen that compared to the polishing by pure CeO₂, The increase in polishing quality of all compound abrasives, which is reflected in lower surface roughness, is accompanied by varying degrees of reduction in polishing rate. In this work, the proposed strategy suggests that the MRR obtained by PS-Ce-Nd abrasive in PCMP is up to 174 nm/min, which is almost two times higher than those of pure CeO₂ (97 nm/min), PS/PANI/CeO₂ (81 nm/min), and PS/D-mSiO₂ (72 nm/min), etc. The improved MRR can be attributed to the enhanced photocatalytic activity and the generation of defects such as V_O and Ce³⁺ caused by doping. However, it is also obtained at the expense of the polishing quality, and the polished surface roughness obtained in this work (Ra: 0.36 nm) is

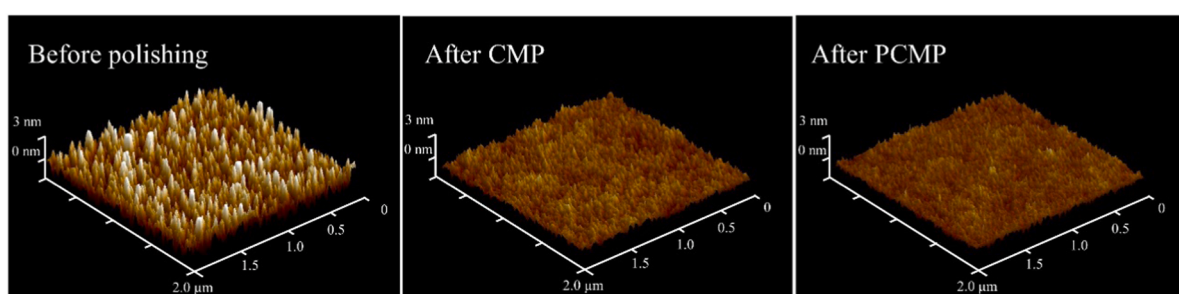


Fig. 10. 3D-AFM images of the surface (a) before polishing and after (b) CMP and (c) PCMP with PS-Ce-Nd abrasives.

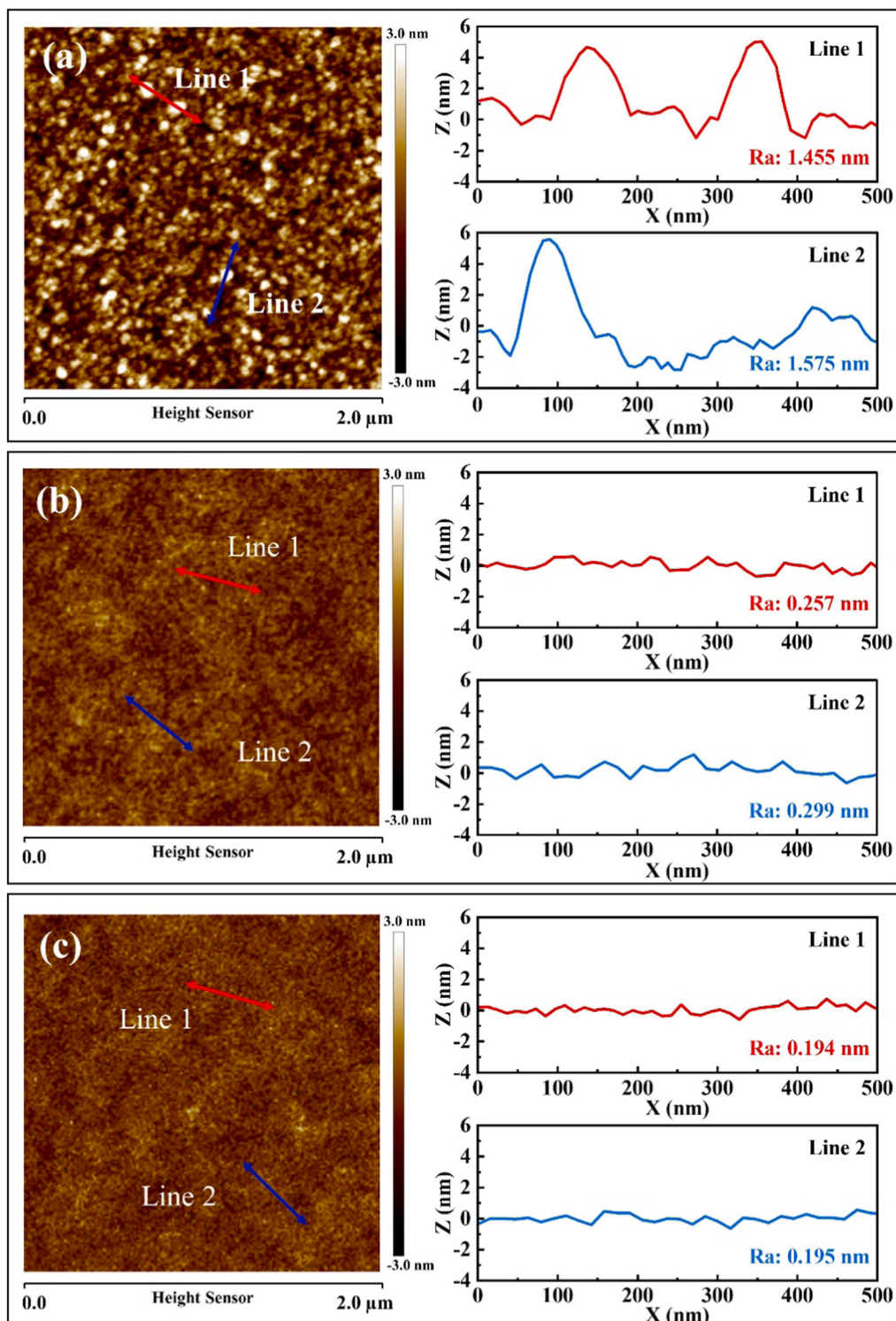


Fig. 11. 2D-AFM images and Line-scan profiles of the surface (a) before polishing and after (b) CMP and (c) PCMP with PS-Ce-Nd abrasives.

Table 4
Results of polishing experiments.

	Initial surface	PS-Ce-Nd	
		CMP	PCMP
MRR (nm/min)	–	65.8 ± 3.7	174.3 ± 7.6
Ra (nm)	0.82 ± 0.01	0.46 ± 0.01	0.36 ± 0.05
Line 1 (nm)	1.455	0.257	0.194
Line 2 (nm)	1.575	0.299	0.195

unsatisfactory concerning the previously published abrasives. Therefore, the proper and dynamic balance between mechanical and chemical action in the material removal process needs to be optimized in the next step to achieve more desirable polishing results.

3.4. Mechanistic analysis

Fig. 12 depicts the schematic of the atomic structure of Nd-doped CeO_2 , where each cerium cation is coordinated by eight oxygen anions

Table 5

Statistics of polishing results for different composite materials.

Abrasives	Ra (nm)	RMS (nm)	MRR (nm/min)	reference
CeO ₂		0.25	97	[39]
PS/CeO ₂	0.11	0.15	26	[40]
PS/PANI/CeO ₂	0.12	0.16	81	[25]
PS/SiO ₂		0.217	126.2	[41]
PS/D-mSiO ₂	–	0.26	72	[42]
PS/W-mSiO ₂	–	0.19	62	[43]
PS-Ce-Nd	0.36	–	174	This work

(Fig. 12 b). After the introduction of Nd ions, the exposed Ce ions on the surface are partially replaced by those Nd³⁺ (Fig. 12 a), leading to a decrease in the total positive charge and oxygen vacancy formation energy (E_{vac}) of CeO₂. Cheng [16] proposed that the E_{vac} for pure CeO₂ calculated by DFT is 3.27 eV per vacancy, while for Nd-doped CeO₂, it is drastically reduced to 1.00 eV. Such a large reduction in E_{vac} facilitated the escape of surface oxygen from the crystal structure to form V_O and the associated change from Ce⁴⁺ to Ce³⁺ for maintaining electro-neutrality (Fig. 12 c), as demonstrated by the Raman test. In addition, the as-created V_O can serve as a trapping center for photogenerated electrons to form a doped transition state between the conduction band (CB) and valence band (VB) of CeO₂ (Fig. 12), resulting in a narrow band gap of the photocatalyst [37], consistent with the UV-vis DRS. The transition state caused by doping can effectively limit the compounding of photogenerated charges, and prolong the lifetime of photogenerated carriers in the migration process, contributing to improved photocatalytic performance.



Based on the results of structural characterization and photocatalytic evaluation experiments (PL, DRS, Raman, XPS, and the test of CR degradation), a reasonable polishing mechanism of PS-Ce-Nd was proposed. The surface of silica wafer was firstly softened by the strong oxide species produced by the photocatalysis, and subsequently removed by a synergistic mechanical and chemical process, as detailed below.

As shown in Fig. 13 (a), the light-generated carriers migrated to the abrasive surface by electric field or diffusion, where they reacted further with the adsorbed substances on the surface in reduction and oxidation reactions, producing oxidation active species (·OH, ·O²⁻, etc). Subsequently, the initial surface was oxidized to form a softer layer that can be more easily removed. Fig. 13 (b) revealed that the material removal mechanism of CeO₂ on SiO₂ is primarily associated with the dynamic formation and breakage of the Ce-O-Si bond. In the weakly alkaline polishing slurry, the hydrolysis reaction of SiO₂ could occur to form numerous Si-O⁻ sites (reaction 8). On the other hand, V_O on the surface of CeO₂ can react with water to create surface hydroxyl groups, which in turn react with Si-O⁻ sites on the SiO₂ film to generate Ce-O-Si bonds (reaction 9) [22]. Subsequently, the relatively weak Si-O-Si bond might be broken by mechanical motion between the particulate abrasive and the hydrated layer, and the lump of SiO₂ on the softer layer will be removed, which is the “chemical-tooth” model proposed by Cook [8]. Many experimental studies and theoretical simulations [16,20,21,38] substantiated that Ce³⁺ and V_O in CeO₂ abrasives facilitate the frictional

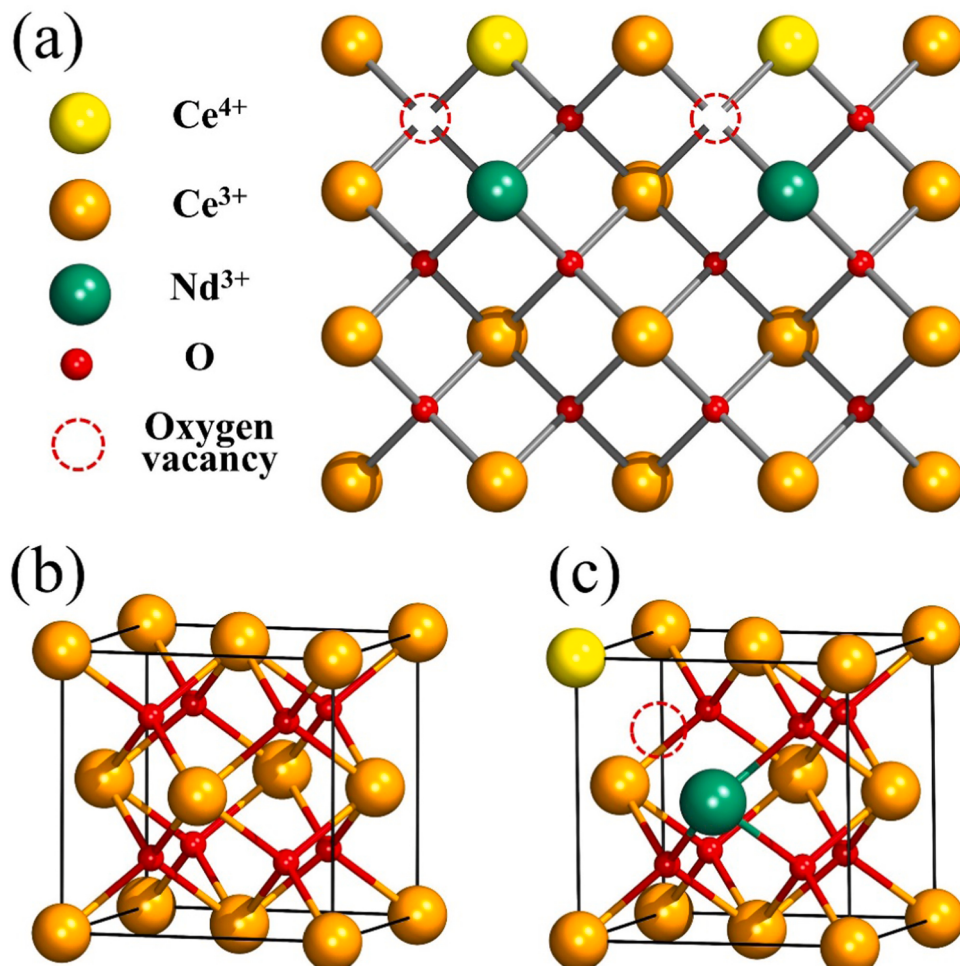
**Fig. 12.** The atomic structure of Nd-doped CeO₂ surfaces.



Fig. 13. Schematics of (a) the surface modification and (b) the material removal during CMP/PCMP processes using PS-Ce-Nd abrasives.

chemical activity between CeO₂-SiO₂, thereby improving the material removal efficiency. There is a reliable correlation between the material removal rate and surface defects of CeO₂ (typically Ce³⁺ and V_O).

In summary, the improvements of both photochemical and enriched surface defects are responsible for the enhancements of formation and removal of the chemically softer layer.

4. Conclusion

The core-shell structured polystyrene (PS)/CeO₂ binary composites (core: 85 nm, shell: 10 nm) were synthesized by a simple method, and RE (RE = La, Nd, and Eu) was successfully doped in CeO₂. The Nd-doped PS/CeO₂ exhibited superior photocatalytic performance with a reduced band gap from 3.24 to 3.20 eV according to the UV-vis DRS, hence applied to investigate the effect of photocatalysis on silicon wafer polishing. The stability of the slurry was significantly modified by the addition of PVP, which remained stable for up to 7 days. With the introduction of photocatalysis, the MRR of PS-Ce-Nd abrasives was effectively increased by 163% (174 vs. 66 nm/min), while the Ra in localized areas was only 0.36 nm. In the future, the optimal slurry composition and polishing process to improve the polishing performance will be further investigated, and the actual polishing performance of the remaining two doped abrasives will be determined.

CRediT authorship contribution statement

Yongyu Fan, Designed the experiments, prepared and analyzed materials, wrote the paper. Jie Jiao, Formal analysis, Data curation. Lang Zhao and Jinkui Tang guided the experiments, reviewed the paper. Supervision, Project administration. Funding acquisition.

Declaration of Competing Interest

The authors declare that they have no known competing financial interests or personal relationships that could have appeared to influence the work reported in this paper.

Data Availability

No data was used for the research described in the article.

Acknowledgments

This work was financially supported Jilin Province Science and Technology Development Program (Grants YDZJ202201ZYTS518) and Special Science and Technology Project of Northern Rare Earth (BFXT-2022-D-0021).

References

- [1] Z. Zhang, Z. Shi, Y. Du, Z. Yu, L. Guo, D. Guo, A novel approach of chemical mechanical polishing for a titanium alloy using an environment-friendly slurry, *Appl. Surf. Sci.* 427 (2018) 409–415, <https://doi.org/10.1016/j.apsusc.2017.08.064>.
- [2] L. Liu, Z. Zhang, B. Wu, W. Hu, F. Meng, Y. Li, A review: green chemical mechanical polishing for metals and brittle wafers, *J. Phys. D: Appl. Phys.* 54 (2021), 373001, <https://doi.org/10.1088/1361-6463/ac0c4a>.
- [3] Z. Zhang, J. Cui, J. Zhang, D. Liu, Z. Yu, D. Guo, Environment friendly chemical mechanical polishing of copper, *Appl. Surf. Sci.* 467–468 (2019) 5–11, <https://doi.org/10.1016/j.apsusc.2018.10.133>.
- [4] L. Liao, Z. Zhang, F. Meng, D. Liu, B. Wu, Y. Li, W. Xie, A novel slurry for chemical mechanical polishing of single crystal diamond, *Appl. Surf. Sci.* 564 (2021), 150431, <https://doi.org/10.1016/j.apsusc.2021.150431>.
- [5] Z. Zhang, L. Liao, X. Wang, W. Xie, D. Guo, Development of a novel chemical mechanical polishing slurry and its polishing mechanisms on a nickel alloy, *Appl. Surf. Sci.* 506 (2020), 144670, <https://doi.org/10.1016/j.apsusc.2019.144670>.
- [6] Z. Zhang, J. Liu, W. Hu, L. Zhang, W. Xie, L. Liao, Chemical mechanical polishing for sapphire wafers using a developed slurry, *J. Manuf. Syst.* 62 (2021) 762–771, <https://doi.org/10.1016/j.jmapro.2021.01.004>.
- [7] W. Xie, Z. Zhang, L. Liao, J. Liu, H. Su, S. Wang, D. Guo, Green chemical mechanical polishing of sapphire wafers using a novel slurry, *Nanoscale* 12 (2020) 22518–22526, <https://doi.org/10.1039/DONR04705H>.
- [8] L.M. Cook, Chemical processes in glass polishing, *J. Non Cryst. Solids* 120 (1990) 152–171, [https://doi.org/10.1016/0022-3093\(90\)90200-6](https://doi.org/10.1016/0022-3093(90)90200-6).
- [9] L.Y. Wang, K.L. Zhang, Z.T. Song, S.L. Feng, Ceria concentration effect on chemical mechanical polishing of optical glass, *Appl. Surf. Sci.* 253 (2007) 4951–4954, <https://doi.org/10.1016/j.apsusc.2006.10.074>.
- [10] H. Chen, L. Zhang, M. Li, G. Xie, Synthesis of core-shell micro/nanoparticles and their tribological application: a review, *Materials* 13 (2020) 4590, <https://doi.org/10.3390/ma13204590>.
- [11] A.L. Chen, Y.Y. Wang, J.W. Qin, Z.F. Li, Chemical mechanical polishing for SiO₂ film using polystyrene@ceria (PS@CeO₂) core-shell nanocomposites, *J. Inorg. Organomet. Polym. Mater.* 25 (2015) 1407–1413, <https://doi.org/10.1007/s10904-015-0253-y>.
- [12] Y. Chen, R. Long, Polishing behavior of PS/CeO₂ hybrid microspheres with controlled shell thickness on silicon dioxide CMP, *Appl. Surf. Sci.* 257 (2011) 8679–8685, <https://doi.org/10.1016/j.apsusc.2011.05.047>.
- [13] Y. Chen, Z.N. Li, N.M. Miao, Polymethylmethacrylate (PMMA)/CeO₂ hybrid particles for enhanced chemical mechanical polishing performance, *Tribol. Int.* 82 (2015) 211–217, <https://doi.org/10.1016/j.triboint.2014.10.013>.
- [14] Y. Chen, Z.G. Chan, Preparation and oxide CMP performance of inorganics coated polystyrene composite particles, *Adv. Mater. Res.* 189–193 (2011) 273–278, <https://doi.org/10.4028/www.scientific.net/AMR.189-193.273>.
- [15] Y. Chen, W.B. Mu, J.X. Lu, Young's modulus of PS/CeO₂ composite with core/shell structure microspheres measured using atomic force microscopy, *J. Nanopart. Res.* 14 (2012) 696, <https://doi.org/10.1007/s11051-011-0696-1>.
- [16] J. Cheng, S. Huang, Y. Li, T.Q. Wang, L.L. Xie, X.C. Lu, RE (La, Nd and Yb) doped CeO₂ abrasive particles for chemical mechanical polishing of dielectric materials: experimental and computational analysis, *Appl. Surf. Sci.* 506 (2020), 144668, <https://doi.org/10.1016/j.apsusc.2019.144668>.
- [17] J. Cheng, S. Huang, X.C. Lu, Preparation of surface modified ceria nanoparticles as abrasives for the application of chemical mechanical polishing (CMP), *Ecs. J. Solid. State Sci. Technol.* 9 (2020), 024015, <https://doi.org/10.1149/2162-8777/ab7098>.
- [18] B. Gao, W.J. Zhai, Q. Zhai, M.Z. Zhang, Novel polystyrene/CeO₂-TiO₂ multicomponent core/shell abrasives for high-efficiency and high-quality photocatalytic-assisted chemical mechanical polishing of reaction-bonded silicon carbide, *Appl. Surf. Sci.* 484 (2019) 534–541, <https://doi.org/10.1016/j.apsusc.2019.04.037>.
- [19] Y. Chen, C.Z. Zuo, Z.F. Li, A.L. Chen, Design of ceria grafted mesoporous silica composite particles for high-efficiency and damage-free oxide chemical mechanical polishing, *J. Alloy. Compd.* 736 (2018) 276–288, <https://doi.org/10.1016/j.jallcom.2017.11.112>.
- [20] Y. Chen, W.J. Cai, W.Y. Wang, A.L. Chen, Preparation, characterization, and application of dendritic silica-supported samarium-doped ceria nanoparticles in ultra-precision polishing for silica films, *J. Nanopart. Res.* 21 (2019) 226, <https://doi.org/10.1007/s11051-019-4684-1>.
- [21] A.L. Chen, Y.H. Duan, Z.Y. Mu, W.J. Cai, Y. Chen, Meso-silica/Erbium-doped ceria binary particles as functionalized abrasives for photochemical mechanical

- polishing (PCMP), *Appl. Surf. Sci.* 550 (2021), 149353, <https://doi.org/10.1016/j.apsusc.2021.149353>.
- [22] A. Chen, S. Wang, J. Pan, T. Wang, Y. Chen, Development of Zr- and Gd-doped porous ceria (CeO_2) abrasives for achieving high-quality and high-efficiency oxide chemical mechanical polishing, *Ceram. Int.* 48 (2022) 14039–14049, <https://doi.org/10.1016/j.ceramint.2022.01.289>.
- [23] E. Kim, J. Lee, C. Bae, H. Seok, H.-U. Kim, T. Kim, Effects of trivalent lanthanide (La and Nd) doped ceria abrasives on chemical mechanical polishing, *Powder Technol.* 397 (2022), <https://doi.org/10.1016/j.powtec.2021.11.069>.
- [24] T.Y. Wang, Y. Chen, A.L. Chen, Y. Chen, Development of carbon sphere/ceria (CS/CeO₂) heterostructured particles and their applications to functional abrasives toward photochemical mechanical polishing, *Appl. Surf. Sci.* 593 (2022), 153449, <https://doi.org/10.1016/j.apsusc.2022.153449>.
- [25] A. Chen, T. Wang, Y. Chen, S. Wang, Y. Chen, Development of polystyrene/polyaniline/ceria (PS/PANI/CeO₂) multi-component abrasives for photochemical mechanical polishing/planarization applications, *Appl. Surf. Sci.* 575 (2022), 151784, <https://doi.org/10.1016/j.apsusc.2021.151784>.
- [26] H. Zhenxing, Y. Xiaowei, L. Junliang, Y. Yuping, W. Ling, Z. Yanwei, An investigation of the effect of sodium dodecyl sulfate on quasi-emulsifier-free emulsion polymerization for highly monodisperse polystyrene nanospheres, *Eur. Polym. J.* 47 (2011) 24–30, <https://doi.org/10.1016/j.eurpolymj.2010.09.036>.
- [27] Y. Chen, Z.N. Li, N.M. Miao, Synergetic effect of organic cores and inorganic shells for core/shell structured composite abrasives for chemical mechanical planarization, *Appl. Surf. Sci.* 314 (2014) 180–187, <https://doi.org/10.1016/j.apsusc.2014.06.166>.
- [28] S.Y. Lu, D. Xiang, Y.Y. Fan, Y.Q. Ma, L. Zhao, Highly efficient removal of malachite green from water by ZnO/NiO/CeO₂ nanocomposite, *Appl. Nanosci.* 12 (2022) 2241–2254, <https://doi.org/10.1007/s13204-022-02491-w>.
- [29] K.A. Shuhailath, V. Linsha, S.N. Kumar, K.B. Babitha, A.A. Peer Mohamed, S. Ananthakumar, Photoactive, antimicrobial CeO₂ decorated AlOOH/PEI hybrid nanocomposite: a multifunctional catalytic-sorbent for lignin and organic dye (vol 6, pg 54357, 2016), 44773–44773, *RSC Adv.* 10 (2020), <https://doi.org/10.1039/dora90136a>.
- [30] P. Latha, S. Karuthapandian, Novel, facile and swift technique for synthesis of CeO₂ nanocubes immobilized on zeolite for removal of CR and MO Dye, *J. Clust. Sci.* 28 (2017) 3265–3280, <https://doi.org/10.1007/s10876-017-1292-z>.
- [31] R.C. Evans, *An Introduction to Crystal Chemistry*, second ed., Cambridge University Press, 1976.
- [32] C. Sun, H. Li, H. Zhang, Z. Wang, L. Chen, Controlled synthesis of CeO₂ nanorods by a solvothermal method, *Nanotechnology* 16 (2005) 1454–1463, <https://doi.org/10.1088/0957-4484/16/9/006>.
- [33] M.Y. Cui, X.Q. Yao, W.J. Dong, K. Tsukamoto, C.R. Li, Template-free synthesis of CuO-CeO₂ nanowires by hydrothermal technology, *J. Cryst. Growth* 312 (2010) 287–293, <https://doi.org/10.1016/j.jcrysgro.2009.10.027>.
- [34] D. Chanhei, B. Inceesungvorn, N. Wetchakun, S. Phanichphant, A. Nakaruk, P. Koshy, C.C. Sorrell, Photocatalytic activity under visible light of Fe-doped CeO₂ nanoparticles synthesized by flame spray pyrolysis, *Ceram. Int.* 39 (2013) 3129–3134, <https://doi.org/10.1016/j.ceramint.2012.09.093>.
- [35] J.H. Park, C.H. Jung, K.J. Kim, D. Kim, H.R. Shin, J.-E. Hong, K.T. Lee, Enhancing bifunctional electrocatalytic activities of oxygen electrodes via incorporating highly conductive Sm³⁺ and Nd³⁺ double-doped ceria for reversible solid oxide cells, *ACS Appl. Mater. Interfaces* 13 (2021) 2496–2506, <https://doi.org/10.1021/acsmami.0c17238>.
- [36] J.J. Carey, M. Nolan, Dissociative adsorption of methane on the Cu and Zn doped (111) surface of CeO₂, *Appl. Catal. B: Environ.* 197 (2016) 324–336, <https://doi.org/10.1016/j.apcatb.2016.04.004>.
- [37] B. Xu, H. Yang, Q.T. Zhang, S.S. Yuan, A. Xie, M. Zhang, T. Ohno, Design and synthesis of Sm, Y, La and Nd-doped CeO₂ with a broom-like hierarchical structure: a photocatalyst with enhanced oxidation performance, *Chemcatchem* 12 (2020) 2638–2646, <https://doi.org/10.1002/cetc.201902309>.
- [38] E. Kim, J. Hong, S. Hong, C. Kanade, H. Seok, H.-U. Kim, T. Kim, Improvement of oxide removal rate in chemical mechanical polishing by forming oxygen vacancy in ceria abrasives via ultraviolet irradiation, *Mater. Chem. Phys.* 273 (2021), 124967, <https://doi.org/10.1016/j.matchemphys.2021.124967>.
- [39] A.L. Chen, Y.Y. Wang, J.W. Qin, Z.F. Li, Chemical mechanical polishing for SiO₂ film using polystyrene/ceria (PS@CeO₂) core-shell nanocomposites, *J. Inorg. Organomet. P.* 25 (2015) 1407–1413, <https://doi.org/10.1007/s10904-015-0253-y>.
- [40] W. Wang, Y. Chen, A. Chen, X. Ma, Composite particles with dendritic mesoporous-silica cores and nano-sized CeO₂ shells and their application to abrasives in chemical mechanical polishing, *Mater. Chem. Phys.* 240 (2020), 122279, <https://doi.org/10.1016/j.matchemphys.2019.122279>.
- [41] Y. Chen, Z. NaLi, Z.T. Shan, Gq Min, Effect of the core size of the core /shell structured PS/SiO₂ composite abrasives on oxide-CMP behavior, *J. Funct. Mater.* 45 (2014), 0-0, https://kns.cnki.net/kcms/detail/detail.aspx?dbcode=CJFD&dbname=CJFD2014&filename=GNCL201419025&uniplatform=NZKPT&v=Mu4FxyGogxjZ-cWzcQ3kkFYyW19pn_uJeJjsKsq39U9Qq2S8G2sXPhfzUrU-E5.
- [42] A. Chen, X. Ma, W. Cai, Y. Chen, Polystyrene-supported dendritic mesoporous silica hybrid core/shell particles: controlled synthesis and their pore size-dependent polishing behavior, *J. Mater. Sci.* 55 (2020) 577–590, <https://doi.org/10.1007/s10853-019-03960-4>.
- [43] A. Chen, J. Qin, Z. Li, Y. Chen, Engineering functionalized PS/mSiO₂ composite particles with controlled meso-shell thickness for chemical mechanical planarization applications, *J. Mater. Sci.* 28 (2017) 284–288, <https://doi.org/10.1007/s10854-016-5522-1>.